ELSEVIER

Chemical Engineering Journal 133 (2007) 247–256

Chemical Engineering Journal

www.elsevier.com/locate/cej

An experimental method of examining three-dimensional swirling flows in gas cyclones by 2D-PIV

Zhengliang Liu [a], Ying Zheng [a,*], Lufei Jia [b], Qikai Zhang [a]

[a] *Department of Chemical Engineering, University of New Brunswick, 15 Dineen Drive, P.O. Box 4400, Fredericton, NB, Canada E3B 5A3*
[b] *CANMET Energy Technology Center, 1 Haanel Drive, Ottawa, Ont., Canada K1A 1M1*

Received 29 November 2005; received in revised form 30 January 2007; accepted 14 February 2007

Abstract

With two-dimensional particle image velocimetry (2D-PIV), planar flows can be well examined when there is no out-of-plane (perpendicular to the lightsheet plane) flow motion. In gas cyclones, the turbulent swirling flows are three-dimensional. When they are investigated by 2D-PIV, contamination is introduced into the experimental results due to the existence of considerable out-of-plane velocity caused by the tangential gas motion. In this paper, an experimental method is introduced to investigate the axial and radial velocities by 2D-PIV, followed by the proposed contamination-removing schemes. The contamination on the axial velocity has been efficiently eliminated whereas that on the radial velocity is difficult to evaluate. The radial velocity distribution is then obtained based on a local mass balance calculation. The flow pattern in the dust hopper is also well examined.

Keywords: Particle image velocimetry (PIV); Flow structure; Contamination; Experimental design; Gas cyclones

1. Introduction

Novel technology in energy generation area, such as integrated gasification combined cycle and pressurized fluidized bed combustion, has been booming in recent years. Researchers have realized that there is an imperative need for effective separation of fine particles due to the stringent requirement for resource conservation and sustainable development in environmental protection [1]. As a low-cost unit operation for the removal of solids from gases, cyclone separators are widely used in the petrochemical and process industries for particulate separation. Compared to filters, scrubbers, and settlers in industrial dedusting, cyclone separators have the advantages of simple construction and compactness, easy maintenance, and good flexibility with respect to high temperature and pressure. Efforts have been put into improving the collection efficiency of industrial-scale cyclones for fine particles by many researchers [2–4].

The swirling flows in cyclones which are usually divided into three components in tangential, axial, and radial directions are fluctuant and complex. Extensive investigations of the flow fields have been performed by experimental methods [5–8], numerical simulations [9,10], or both [11,12]. The experimental techniques for observing the swirling flows have been developed from Pitot tubes and hot-wire anemometers (HWA) to non-intrusive techniques such as laser Doppler anemometry (LDA) [5–8]. However, all the aforementioned techniques have a common limitation: they can only make one-point measurement at a time. Particle image velocimetry (PIV) is a new non-intrusive visualization technique that can detect the whole-field velocity at the same time. Unfortunately, the application of PIV for the study of the gas flow in cyclones has not yet been well documented.

When there is no out-of-plane (perpendicular to the illumination lightsheet plane) motion, planar flows can be accurately observed with two-dimensional (2D)-PIV technique. However, contamination will be introduced into the experimental results when the out-of-plane velocity is considerable. With 2D-PIV, the axial and radial velocities in cyclones can be observed simultaneously. But contamination is registered on them due to the prominent tangential velocity in cyclones. To make the PIV results applicable, the contamination should be removed efficiently. The main purpose of this work is to present an experimental method and

* Corresponding author. Tel.: +1 506 4473329; fax: +1 506 4533591.
E-mail address: yzheng@unb.ca (Y. Zheng).

1385-8947/$ – see front matter © 2007 Elsevier B.V. All rights reserved.
doi:10.1016/j.cej.2007.02.015

Nomenclature

a	cyclone inlet height (mm)
b	cyclone inlet width (mm)
d_c	cyclone conical dust outlet diameter (mm)
d_i	cyclone vortex finder diameter (mm)
d_o	cyclone dust outlet diameter (mm)
dT	time separation between two image frames (μs)
D	cyclone cylindrical body diameter (mm)
D_b	cyclone dust hopper body diameter (mm)
H	cyclone conical body height (mm)
I_n	cyclone inlet length (mm)
L	cyclone cylindrical body height (mm)
Q_{z_i}	volumetric axial flow at axial position z_i (m^3/s)
r	radial coordinates
R	radius of cyclone cylindrical body (=D/2) (mm)
Re	Reynolds number
s	extrusive vortex finder height (mm)
S	geometric swirl number
St	Stokes number
U_{in}	inlet air velocity (m/s)
V_r	radial velocity (m/s)
V_t	tangential velocity (m/s)
V_z	axial velocity (m/s)
x	horizontal coordinates
z	vertical/axial coordinates
Z_b	cyclone cylindrical dust hopper height (mm)
Z_c	cyclone conical dust hopper height (mm)
Z_d	cyclone dust outlet height (mm)

Greek symbols

μ	viscosity (Pa s)
ρ	density (kg/m^3)
τ	time (s)

Subscripts

f	air
p	particle

contamination-removing schemes to properly examine the three-dimensional flow in a gas cyclone using the technique of 2D-PIV.

2. Experimental setup

A schematic diagram of the experimental apparatus is depicted in Fig. 1. The air stream was fed into the cyclone through a regenerative blower (Gast R6150J-2) with free airflow capacity of 365 m^3/h. The pressure drop through the cyclone was determined by a U-tube manometer. The inlet airflow rate being measured by a digital Pitot tube (Kimo AMI KS300) was controlled by a throttle valve and a by-pass valve. A thin laser lightsheet illuminated the measured flow field where tracer particles were added by an atomizer (TSI 9306A). The images of tracer particles, carrying the flow information of the field, were recorded by a CCD camera and transferred to the computer for analysis.

2.1. Cyclone geometry

The cyclone investigated in this study is made of Plexiglas, as shown in Fig. 2. All dimensions (units in mm) of the cyclone are listed in Table 1. The air was introduced into the cyclone tangentially through a scroll type inlet. It spiraled downward till reaching the conical section, and then the air exhausted through the vortex finder at the top of the cyclone.

The axial and radial velocity components were measured. Measurements were performed across both 0–180° and 90–270° sections in the cylindrical and conical separation zones and in the dust hopper area. The angular positions are indicated in the top view in Fig. 2(b). The size and position of the observing fields (S-I, S-II, and S-III) are shown in Table 1 and Fig. 2(a), respectively.

A Reynolds number, Re, as well as a geometric swirl parameter, S, usually characterizes the swirling flow in a cyclone. Both parameters can be expressed in terms of geometrical factors and inlet conditions [13]:

$$Re = \frac{\rho_f U_{in} b}{\mu_f}, \quad (1)$$

$$S = \frac{\pi d_i D}{4ab}. \quad (2)$$

The swirl number in the cyclone is 2.45. The cyclone was operated at Reynolds number of 2.0×10^4 to 4.2×10^4 with inlet air velocity varying from 7.2 to 15.0 m/s. Detailed operating conditions are listed in Table 2.

2.2. Seeding

Tiny sugar particles (density: 1.58×10^3 kg/m^3, refractive index: 1.54) were generated in a six-jet atomizer (TSI 9306A) by atomizing a 5 wt% sugar solution. Fig. 3 shows the operating principle of the atomizer. High-pressure air forms a high-

Table 1
Dimensions (mm) of the cyclone

a	68
b	46
d_c	60
d_i	65
d_o	30
D	150
D_b	150
I_n	150
L	260
H	330
s	68
Z_b	200
Z_c	150
Z_d	100
S-I	140 × 105
S-II	120 × 90
S-III	140 × 105

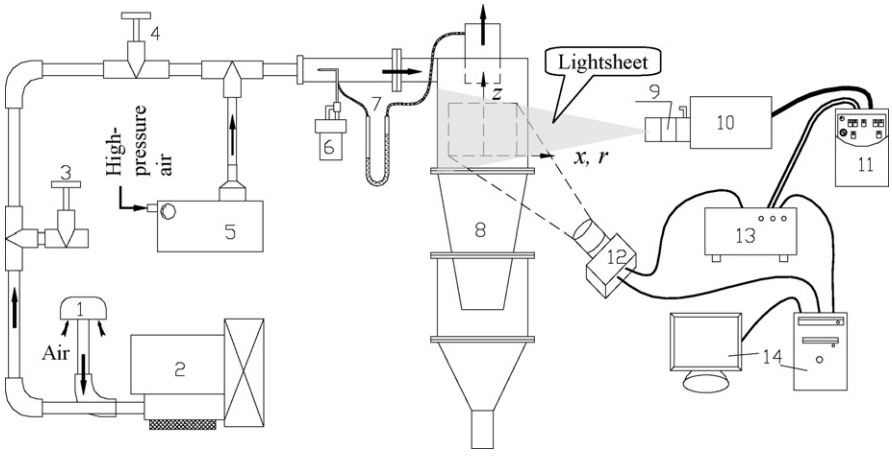

Fig. 1. Schematic diagram of the experimental apparatus and PIV system: (1) air filter, (2) regenerative blower, (3) by-pass valve, (4) throttle valve, (5) atomizer, (6) pitot tube, (7) U-tube manometer, (8) cyclone, (9) lightsheet optics, (10) dual YAG laser, (11) laser controller, (12) CCD camera, (13) synchronizer, and (14) computer system.

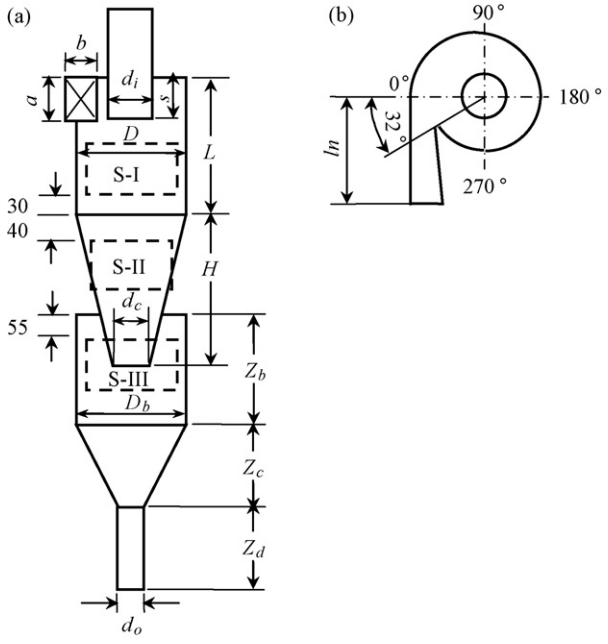

Fig. 2. Cyclone geometry and reference system used.

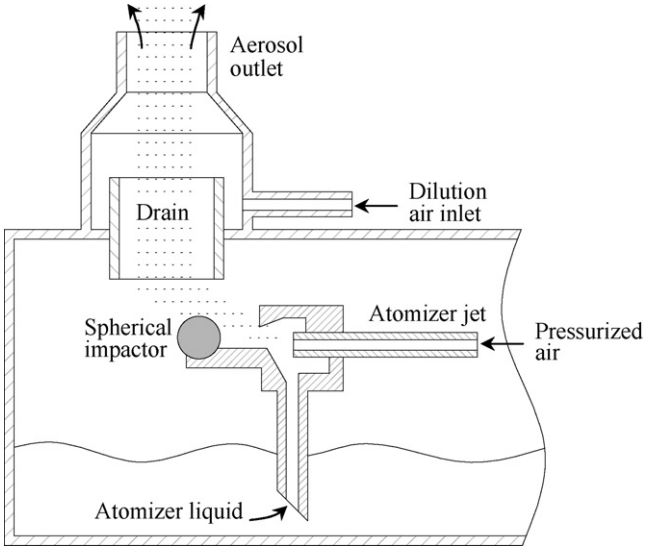

Fig. 3. Schematic drawing of the atomizer.

velocity jet through a 0.015-in.-diameter orifice. The pressure drop from this jet draws liquid up via a narrow tube. The liquid is then broken up into droplets by high-velocity air jets. The resultant larger droplets impinge on the spherical impactor, while the smaller droplets make no contact and form an aerosol that exhausts through a specific outlet. After they are dried by the airflow, the mean size of the sugar particles is around 0.8 μm in diameter. Particle number concentration can be controlled by the number of jets in operation and the input pressure. Higher concentration requires more jets or higher input pressure.

Seeding in a strong swirling flow, such as that found in cyclones, is critical to experiments. First of all, the tracer particles are required to follow the centrifugal airflow strictly. To determine the ability of tracer particles to follow the fluid and how fast the seed particles respond to the flow changes, the particle Stokes number (*St*) is usually introduced. It is defined

Table 2
Operating conditions of the experiments

Inlet air temperature (°C)	Inlet air velocity (m/s)	Inlet *Re* ($\times 10^4$)	Pressure drop through the cyclone (Pa)
40	7.2	2.0	274.5
	9.5	2.6	568.6
	12.2	3.4	980.3
	15.0	4.2	1519.5

as

$$St = \frac{\tau_p}{\tau_f}, \tag{3}$$

where τ_p is the characteristic time of tracer particles or velocity response time and τ_f is the characteristic time of the vortex field:

$$\tau_p = (2\rho_p + \rho_f) \cdot \frac{d_p^2}{36\mu_f} \approx \rho_p \cdot \frac{d_p^2}{18\mu_f} \quad (\text{for } \rho_f \ll \rho_p), \tag{4}$$

$$\tau_f = \frac{R}{V_t} = \frac{D}{2V_t}. \tag{5}$$

When $St < 0.1$, the particle gravity is negligible and the particle motion is considered as representing the fluid behavior [14]. During our experiments, the maximum Stokes number was less than 0.001, which indicates the seeding particles can follow the gas motion without slip.

2.3. PIV system

The PIV system includes an image capture component (CCD cameras and frame grabbers), an illumination component (laser and lightsheet optics), a synchronizer, and an analysis component (computer hardware and software).

A very thin vertical lightsheet with a wavelength of 532 nm is generated by a double-pulsed Nd:YAG laser (New Wave Research Solo III-15) through a set of cylindrical and spherical lenses. The lightsheet illuminates the gas flow in different parts of the cyclone where the investigation is focused. The laser pulse duration is 6 ns with energy of 50 mJ per pulse and repetition rate of 15 Hz. The pulse separation value is selectable to match the gas velocity, during which the particle image displacements are typically less than 1/4 of the interrogation window. The frame straddling technique is applied to measure the flow filed. Two successive exposures of tracer particles to the laser lightsheet are recorded in two separate frames by a high resolution (1600 × 1200 pixel) CCD camera (TSI, model 630151) with a frame rate of 15 Hz. The frame grabber in the computer (Dell workstation, CPU 2.20 GHz) reads the camera images and passes the information to the computer system for processing. The vector fields are calculated by analyzing the recorded images with commercial software Insight 5.0 provided by TSI.

2.4. Perspective correction

Due to its curved wall, the reflection of the lightsheet in the cyclone causes inhomogenous illumination, and the images of tracer particles captured by the CCD camera from outside of the cyclone are distorted by refraction. Fortunately, homogenous illumination was achieved by painting the background of the cyclone wall black. And the distortion was rectified by a two-dimensional perspective correction program provided by TSI.

The theory and process of the perspective correction are as follows: a calibration target with grids of known x and y displacements is put into the cyclone along the lightsheet plane. Calibration equations are generated according to the image of the target captured by the camera. A vector grid field is then defined using the vector pixel locations and the calibration equations. The derivate of the calibration equations at this point is computed and used as the local calibration gradient factors. By assuming the velocity perpendicular to the lightsheet plane equals zero, a vector location in the gas is then mapped into the camera to get the pixel location. The pixel displacement is obtained as

$$\mathrm{d}X = \mathrm{d}x\left(\frac{\delta X}{\delta x}\right) + \mathrm{d}y\left(\frac{\delta X}{\delta z}\right), \tag{6}$$

$$\mathrm{d}Z = \mathrm{d}x\left(\frac{\delta Z}{\delta x}\right) + \mathrm{d}y\left(\frac{\delta Z}{\delta z}\right), \tag{7}$$

where (dx, dz) is displacement in the gas; (dX, dZ) is displacement in the image in pixels; $\delta X/\delta x$, $\delta X/\delta z$, $\delta Z/\delta x$, and $\delta Z/\delta z$ are calibration gradients.

These two equations of two unknowns are solved for the particle displacements in the gas phase:

$$\mathrm{d}x = \frac{\mathrm{d}X/(\delta X/\delta z) - \mathrm{d}Z/(\delta Z/\delta z)}{(\delta X/\delta x)/(\delta X/\delta z) - (\delta Z/\delta x)/(\delta Z/\delta z)}, \tag{8}$$

$$\mathrm{d}z = \frac{\mathrm{d}X/(\delta X/\delta x) - \mathrm{d}Z/(\delta Z/\delta x)}{(\delta X/\delta z)/(\delta X/\delta x) - (\delta Z/\delta z)/(\delta Z/\delta x)}. \tag{9}$$

So the axial and radial gas velocities are

$$V_r = \frac{\mathrm{d}x}{\mathrm{d}T}, \tag{10}$$

$$V_z = \frac{\mathrm{d}z}{\mathrm{d}T}. \tag{11}$$

3. Error discussion

As discussed above, the distortion caused by the curved cyclone wall can be eliminated by the aforementioned perspective correction. At the same time, the strong tangential velocity perpendicular to the lightsheet plane induces contamination on the radial and axial velocities when using 2D-PIV. The following discussion explains how the contamination is generated.

With 2D-PIV, it is assumed that the particle image displacement dX and dZ are only a result of the radial gas motion x and the axial gas motion z, respectively. There is no tangential motion (out-of-plane motion). However, the assumption is not true since a considerable tangential motion does exist in a cyclone. Fig. 4(a) shows the 2D-PIV analysis of a solid surface moving in the positive tangential direction. At the centre of the image, the motion is directly towards the camera, and the measured displacement is zero. Away from the centre of the field of view, the tangential motion is registered in the image as both a dX and a dZ displacement. The measured displacement increases with distance from the camera optical axis, with the arrows pointing away from the optical axis. For the motion in the negative tangential direction, the arrows point toward the optical axis. In contrast, the tangential motion has no contribution to the axial displacement across the horizontal line (marked as line 1) or the radial displacement across the vertical line (marked as line 2) corresponding to the centre lines of the image. So the contamination of the tangential motion on the radial and axial

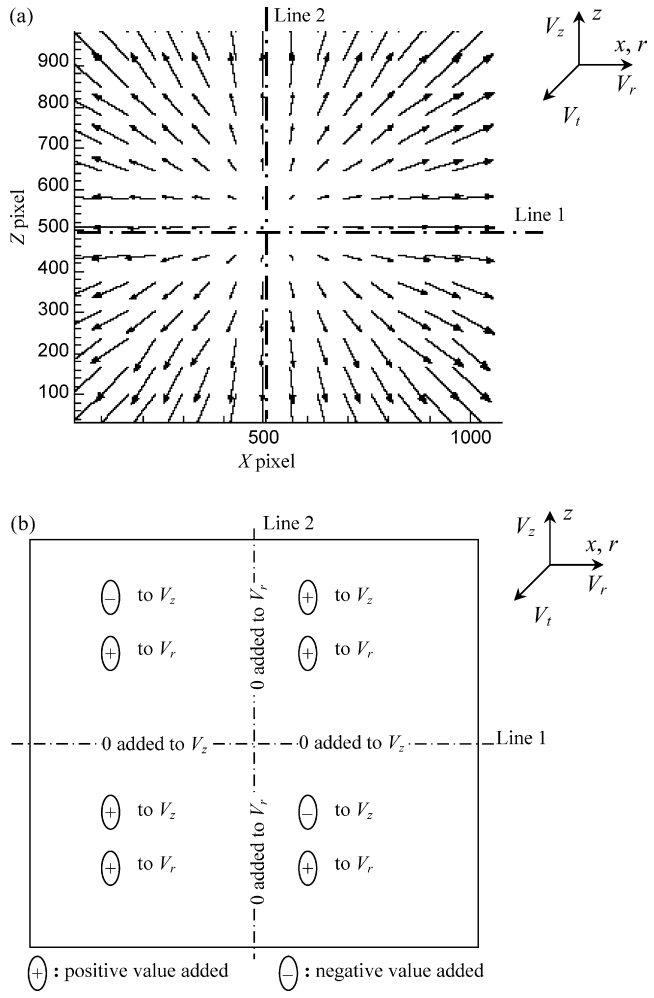

Fig. 4. (a) Measured displacement field for a solid surface moving in the positive tangential direction with 2D-PIV and (b) the contamination of the tangential velocity on the radial and axial velocities in the field of view.

displacements depends on the magnitude, the position, and the direction of the tangential motion.

In the cyclone, there is a negative tangential velocity on the left side of the field of view and a positive one on the right side. The contamination of the tangential velocity on both the radial and axial velocities is illustrated qualitatively in Fig. 4(b), but no quantitative values can be estimated. However, when the tangential velocity is anti-symmetrical with respect to the geometrical axis of the cyclone (line 2), the registered contamination on the axial velocity is also anti-symmetrical while that on the radial velocity is axisymmetrical.

4. Results and discussion

4.1. Crude experimental flow patterns

The instantaneous whole-field gas velocity in both axial and radial directions is determined simultaneously through analyzing the images of the gas flow taken by PIV. Based on the instant velocity values, the time-averaged flow structure can be acquired. Although four different inlet gas velocities (U_{in}) are operated and the instantaneous velocity fields fluctuate from time to time, in the experiments the average flow structures appeared to be similar. The phenomena are observed across both 0–180° and 90–270° axial sections in all parts of the cyclone. The dimensionless axial and radial velocities are obtained by dividing them by the corresponding U_{in}. Since U_{in} shows an insignificant influence on the velocity patterns, the dimensionless velocities are adopted in the following discussion.

Figs. 5 and 6 show typical crude dimensionless gas velocity contour fields in the cylindrical separation zone in both axial and radial directions, respectively. Despite an anisotropic flow structure, it is seen that the axial velocity patterns are similar across both sections. On the other hand, the radial velocity pattern across the section of 0–180° is different from that across the section of 90–270°. Fig. 7(a) and (b) shows the profiles of the dimensionless axial velocity at three axial positions in the cylindrical body. The positions are two symmetrical ones ($z = 10$ and 90 mm) with respect to the horizontal centre line ($z = 50$ mm)

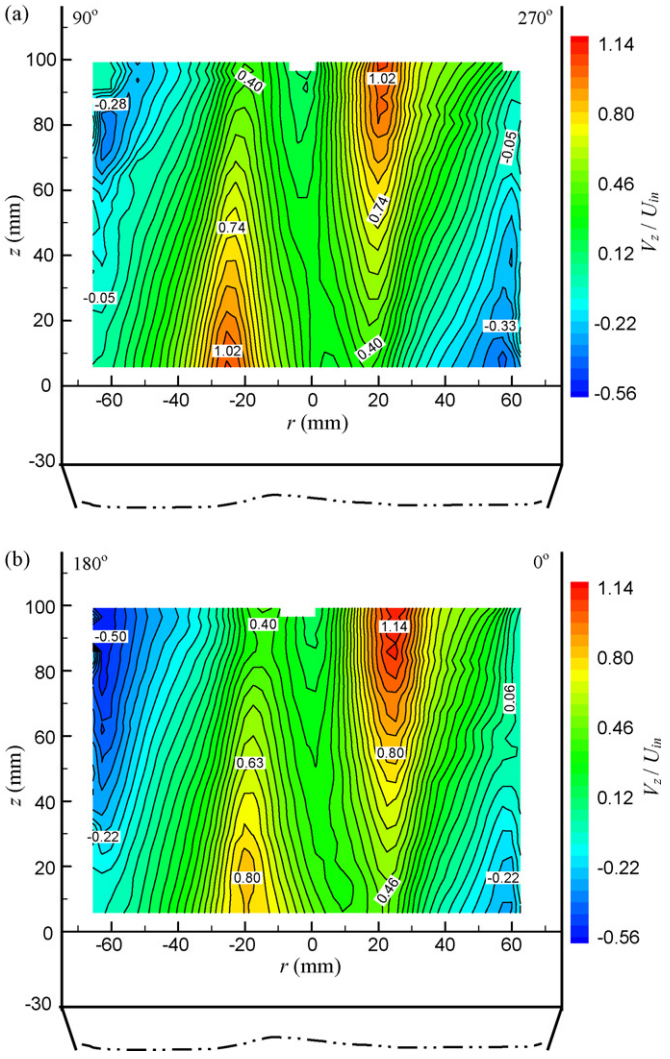

Fig. 5. Contour lines of the axial velocity distribution across both (a) 90–270° and (b) 0–180° axial sections in the cylindrical body. (For interpretation of the references to colour in this artwork, the reader is referred to the web version of the article.)

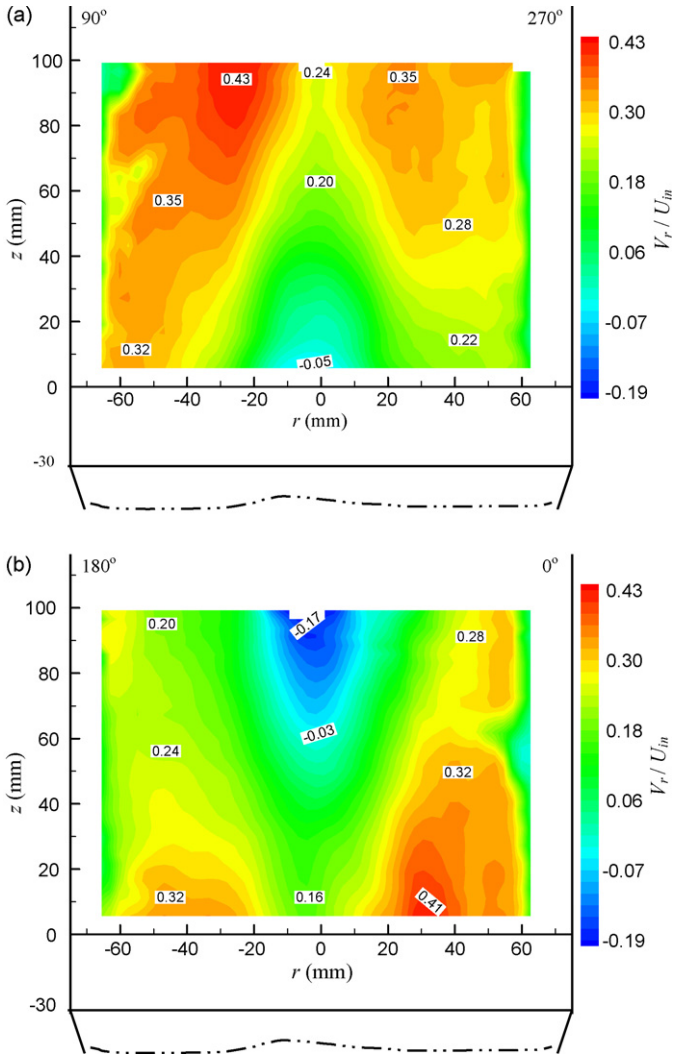

Fig. 6. Contour lines of the radial velocity distribution across both (a) 90–270° and (b) 0–180° axial sections in the cylindrical body. (For interpretation of the references to colour in this artwork, the reader is referred to the web version of the article.)

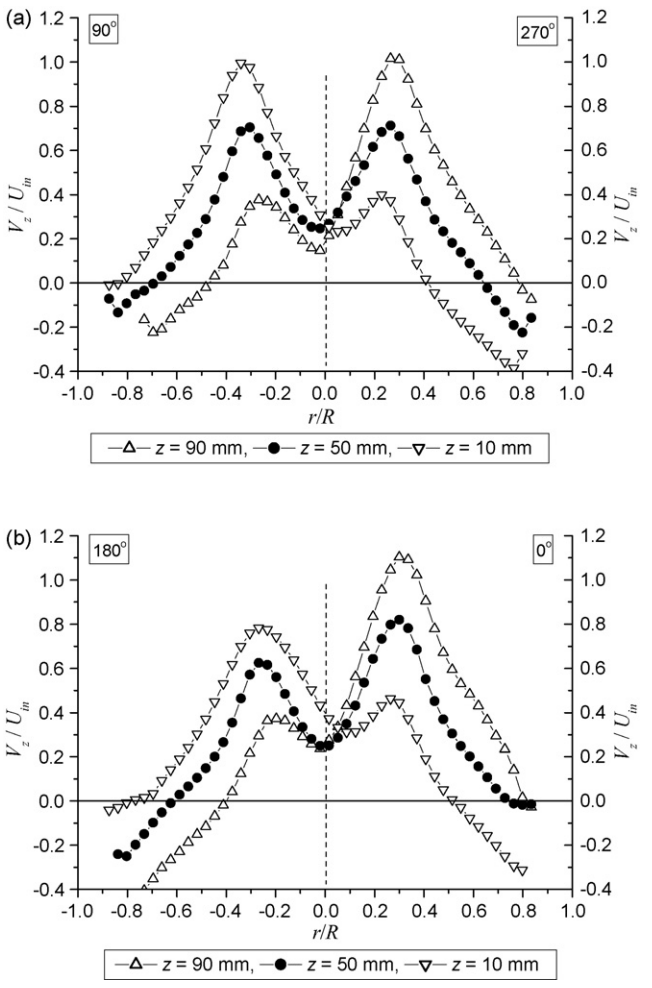

Fig. 7. The profiles of the dimensionless axial velocity across both (a) 90–270° and (b) 0–180° axial sections in the cylindrical body.

in the field of view. For the bimodal distribution of the axial velocity, the right hump is higher than the left one at the upper position ($z = 90$ mm) whereas the converse occurs at the lower position ($z = 10$ mm). The same phenomena are also observed in the conical separation zone. These profiles with uneven humps are predictable from the discussion about the registration of contamination caused by the tangential velocity in Section 3. On the other hand, in the centre of the field of view ($z = 50$ mm) where the axial velocity is free of contamination, the profile in Fig. 7(a) (across the section of 90–270°) has a good symmetrical shape with respect to the geometrical axis of the cyclone, but this does not happen to the section of 0–180° in Fig. 7(b).

4.2. Contamination-removing methods

In Fig. 7, the profiles of the left side to the geometrical axis of the cyclone can be described by

$$(\tilde{V}_z)_{l,z_i}|_{r/R} = [(\tilde{V}_z)_{l,z_i}|_{r/R}]_T + (\Delta\tilde{V}_z)_{l,z_i}|_{r/R}. \quad (12)$$

The profiles of the right side is

$$(\tilde{V}_z)_{r,z_i}|_{r/R} = [(\tilde{V}_z)_{r,z_i}|_{r/R}]_T + (\Delta\tilde{V}_z)_{r,z_i}|_{r/R}, \quad (13)$$

where $\tilde{V}_z = V_z/U_{\text{in}}$ is the dimensionless axial velocity; $\Delta\tilde{V}_z$ the error caused by the contamination of the tangential velocity on the axial velocity; l the left side; r the right side; r/R the dimensionless radial position; z_i the axial position; and T is the true value of the axial velocity.

Previous research [5,15,16] reported that the tangential velocity is axisymmetrical and remains closely the same in the axial direction in the cylindrical separation zone. According to the discussion in Section 3, it is reasonable to assume that the contamination on the axial velocity is anti-symmetrical with respect to both vertical and horizontal centre lines in the field of view. Therefore, the contamination can be eliminated by mathematic methods as stated below.

4.2.1. Method 1

For those sections where the hypothesis of axisymmetric profiles of the axial velocity distribution is applicable, we get $[(\tilde{V}_z)_{l,z_i}|_{r/R}]_T = [(\tilde{V}_z)_{r,z_i}|_{r/R}]_T$. Since the contamination is anti-symmetrical with respect to the vertical centerline

$((\Delta\tilde{V}_z)_{l,z_i}|_{r/R} = -(\Delta\tilde{V}_z)_{r,z_i}|_{r/R})$, it is removed by adding Eqs. (12) and (13). So the contamination-removed profiles can be obtained as follows:

$$[(\tilde{V}_z)_{l,z_i}|_{r/R}]_T = [(\tilde{V}_z)_{r,z_i}|_{r/R}]_T = \frac{1}{2}[(\tilde{V}_z)_{l,z_i}|_{r/R} + (\tilde{V}_z)_{r,z_i}|_{r/R}]. \quad (14)$$

4.2.2. Method 2

As given by the assumption that the contamination is also anti-symmetrical with respect to the horizontal centerline, we get $(\Delta\tilde{V}_z)_{l,z_1}|_{r/R} = -(\Delta\tilde{V}_z)_{l,z_2}|_{r/R}$ and $(\Delta\tilde{V}_z)_{r,z_1}|_{r/R} = -(\Delta\tilde{V}_z)_{r,z_2}|_{r/R}$, where z_1 and z_2 refer to two symmetrical axial positions regarding to the horizontal centerline in the field of view. Then, the contamination can be eliminated by adding the profiles across axial positions z_1 and z_2 (such as $z = 90$ and 10 mm in Fig. 7):

$$[(\tilde{V}_z)_l|_{r/R}]_T = \frac{1}{2}[(\tilde{V}_z)_{l,z_1}|_{r/R} + (\tilde{V}_z)_{l,z_2}|_{r/R}], \quad (15)$$

$$[(\tilde{V}_z)_r|_{r/R}]_T = \frac{1}{2}[(\tilde{V}_z)_{r,z_1}|_{r/R} + (\tilde{V}_z)_{r,z_2}|_{r/R}]. \quad (16)$$

For Eqs. (15) and (16), it is assumed that the axial velocity profiles are similar across the two symmetrical axial positions z_1 and z_2. Given the previously reported results [16], this assumption is generally reasonable in the cylindrical body of the cyclone. However, it is most likely invalid in the conical region where the axial velocity varies with axial position. In the discussion shown below, Method 2 is only used to eliminate the contamination in the cylindrical body of the cyclone.

4.3. Contamination-removed axial velocity profiles

In the section of 90–270°, due to the symmetrical shape of the curve in the center of the field of view ($z = 50$ mm) where the contamination caused by tangential velocity is negligible, it is conjecturable that the axial velocity profiles across the whole section are axisymmetric. So Method 1 was first used to eliminate the contamination. The contamination-removed profiles are depicted in Fig. 8(a). The coincidence of the curves at three positions in Fig. 8(a) suggests the axial velocities in the whole cylindrical separation body across the section of 90–270° are almost independent of the axial positions. The profile of the contamination being removed with Method 2 is also illustrated as the line with open diamond symbols in Fig. 8(a). The coincidence of this curve with the previous three gives evidence to the assumption of axisymmetric profiles proposed in Method 1, as well as to the conclusion of quite similar axial velocity profiles along the axial direction stated above. Fig. 8(a) also indicates the maximum axial velocity that is around $0.7U_{in}$ occurs at the position of $|r/R| = 0.28$, and the surface of zero axial velocity between the outer down-flowing and the inner upward-flowing gas occurs at $|r/R| = 0.65$. The trough of the upward-flowing velocity in the center of the cyclone is around $0.2U_{in}$.

For the section of 0–180°, it is reasonable to assume, based on the discussion above, that the profiles also keep similar shapes. The curve of axial velocities recorded in the center of the view field, which is at $z = 50$ mm in Fig. 7(b), is reasonably considered as free of contamination. Since the profile is asymmetrical, Method 1 is not applicable here, but Method 2 can be applied. The curves with open symbols in Fig. 8(b) were obtained by Method 2. The coincidence of the curves at different axial positions also indicates quite similar profiles of axial velocity distribution in the section. Fig. 8(b) also shows that high axial velocity occurs at the same positions as across the section of 90–270°.

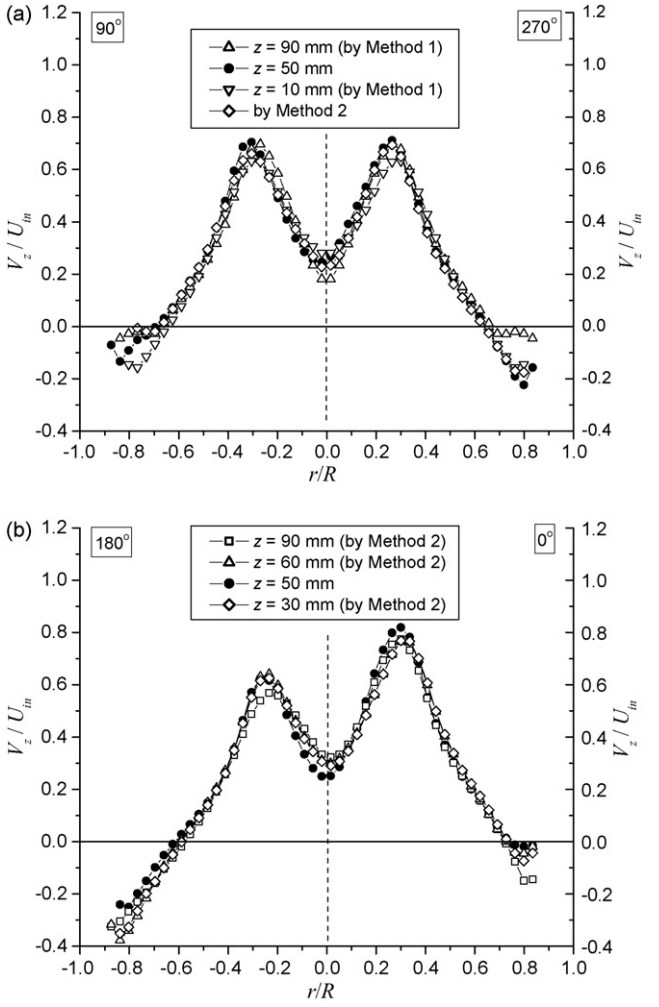

Fig. 8. The contamination-removed profiles of the axial velocity across both (a) 90–270° and (b) 0–180° axial sections in the cylindrical body.

As for the conical separation zone, the axial velocity profiles are symmetrical across both 0–180° and 90–270° axial sections in the centre of the field of view ($z = 45$ mm in Fig. 9) where contamination on the axial velocity is insignificant. So Method 1 was applied to obtain the contamination-removed profiles with the assumption of symmetrical shape, as shown in Fig. 9. The peak value of the maximum axial velocity decreases slightly (from $0.7U_{in}$ to $0.6U_{in}$ in Fig. 9(a)) along the downward axial direction from $z = 80$ to 10 mm in the field of view. At the same time, the trough of the upward-flowing gas velocity in the center increases a little (from $0.36U_{in}$ to $0.45U_{in}$ in Fig. 9(a)), and the locus of zero axial velocity interface moves slightly inwards (from $|r/R| = 0.56$ to 0.46 in Fig. 9(a)).

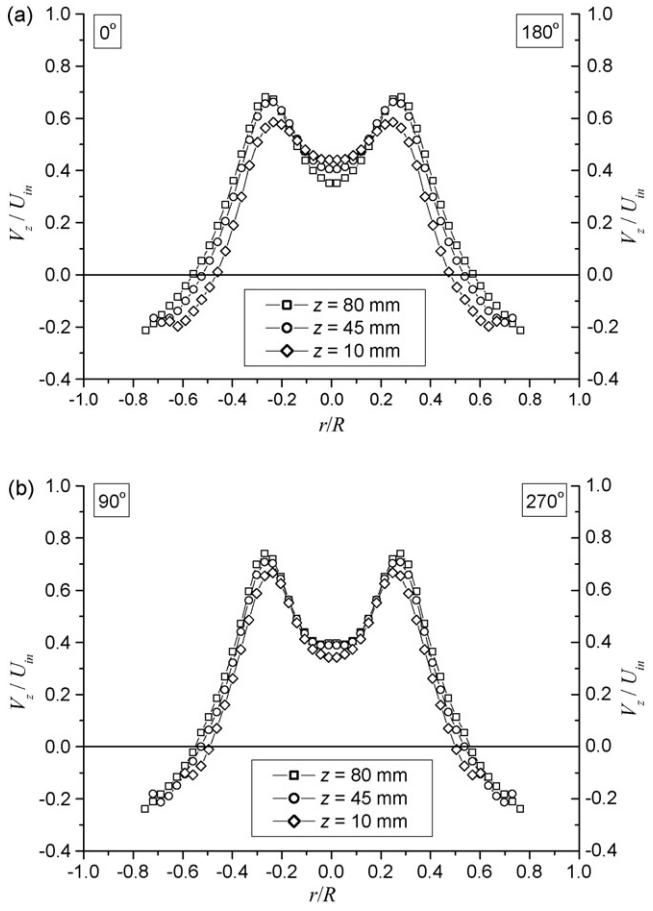

Fig. 9. The contamination-removed profiles of the axial velocity in the conical body.

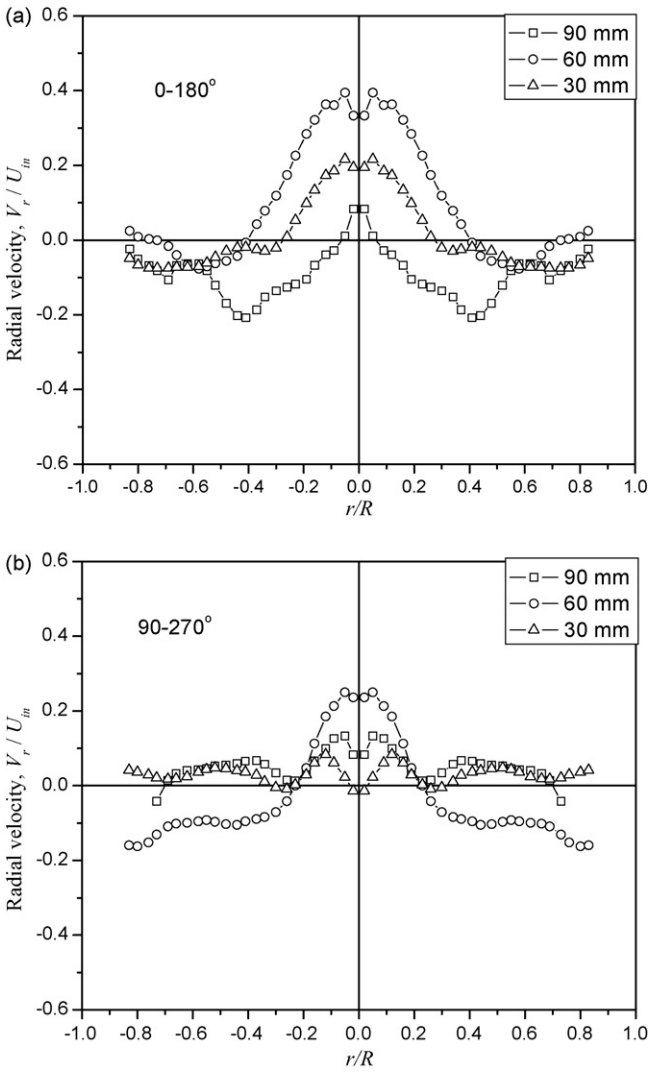

Fig. 10. The radial velocity profiles calculated according to Eq. (17) in the cylindrical body.

4.4. Radial velocity distribution

Based on the discussion in Section 3, the contamination of tangential velocity on the radial velocity is axisymmetrical and positive across both axial sections. Unfortunately, its magnitude is unknown and is hard to be eliminated from the experimental results. However, the crude radial velocity distribution in Fig. 6 indicates that the real distribution is not isotropic and not similar from one axial section to the other.

Previous researchers [6,15] suggested a possible approach to calculate the local radial velocity. Based on the mass balance, the difference of the volumetric axial flows between two adjacent axial positions (z_{i+1} and z_i) gives the average radial flow described by

$$Q_{z_{i+1}} - Q_{z_i} = \left[\int_0^r 2\pi r V_z(r)\,\mathrm{d}r\right]_{z_{i+1}} - \left[\int_0^r 2\pi r V_z(r)\,\mathrm{d}r\right]_{z_i} = 2\pi r \cdot V_\mathrm{r} \cdot (z_{i+1} - z_i). \quad (17)$$

In Eq. (17), it is assumed that the profiles of axial velocity as well as radial velocity across every section in the cyclone are similar.

The radial velocity profiles calculated from the contamination-removed axial velocity by Eq. (17) in cylindrical and conical bodies are depicted in Figs. 10 and 11, respectively. The calculation is based on $z_{i+1} - z_i = 2.7$ mm and the step increment $0.035R$ in the radial direction. Theoretically, Eq. (17) does not apply to the situation of $r = 0$. Hence, the radial velocity at $r = 0$ is represented by the radial velocity at the adjacent positions. The positive values in the profiles represent centrifugal velocity whereas the negative values stand for centripetal velocity. Based on different axial velocity profiles in two sections, the calculated radial velocity distributions are different from each other, as shown in Figs. 10 and 11. It is seen that the centripetal velocity of the gas around the cyclone wall increases when it flows down from the cylindrical body to the conical body. This is predictable because more gas flows from the outer vortex to the inner vortex in the conical body.

4.5. Flow patterns in the dust hopper

In most areas except in the centre area of the dust hopper, the tangential velocity is much weaker. The contamination is,

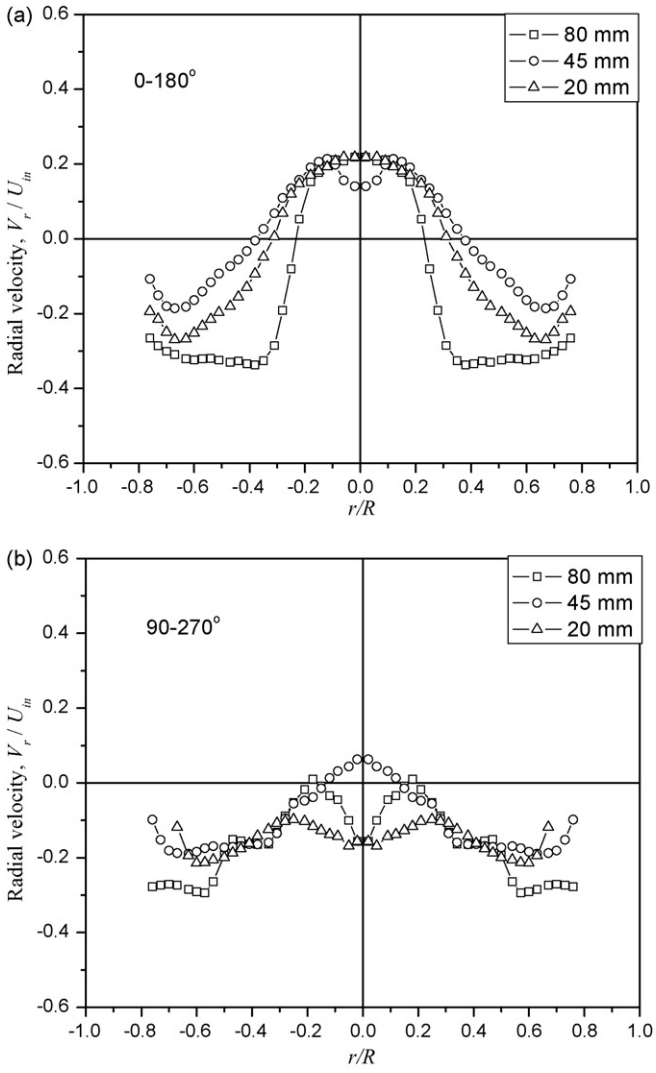

Fig. 11. The radial velocity profiles calculated according to Eq. (17) in the conical body.

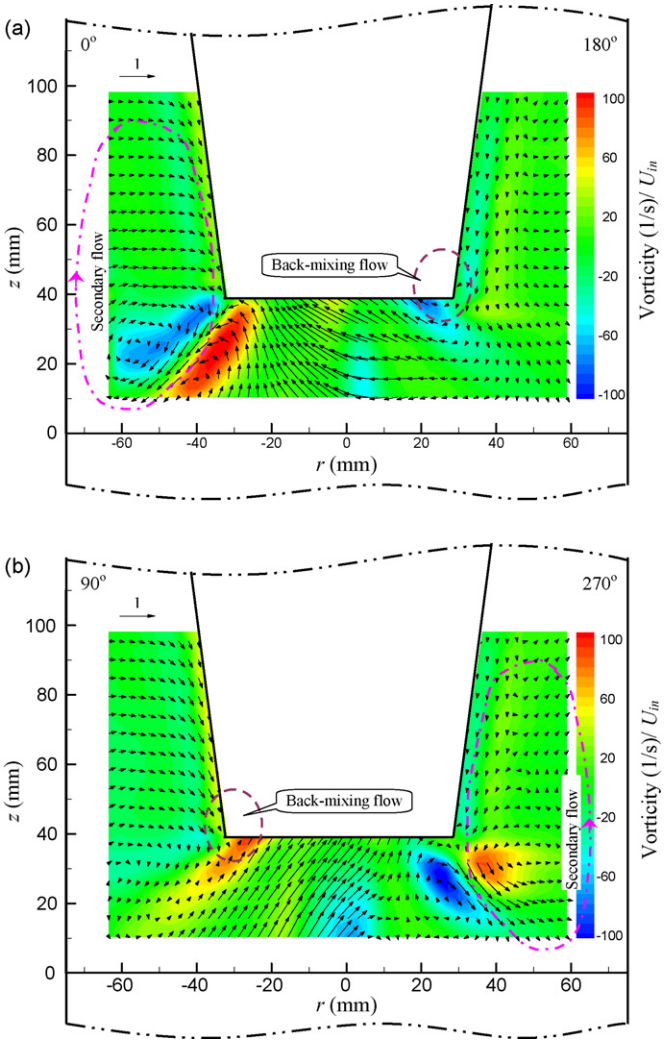

Fig. 12. Time-averaged dimensionless gas velocity vector field superimposed on the vorticity contours across both (a) 0–180° and (b) 90–270° axial sections in dust hopper area when. (For interpretation of the references to colour in this artwork, the reader is referred to the web version of the article.)

therefore, much smaller. Generally, more focus is put on the secondary flow patterns there, as shown in Fig. 12.

Fig. 12(a) and (b) illustrates typical time-averaged dimensionless gas velocity vectors superimposed on the vorticity contour fields across both 0–180° and 90–270° axial sections, respectively, when inlet gas velocity is 7.2 m/s. The outer vortex flow swirls downwards along the inner wall of the conical body. When it reaches the conical dust outlet, the outer vortex expands outwards due to lack of the restriction of the wall, and the gas flows downwards and outwards. Once the gas reaches the wall of the dust hopper, it moves upwards along the inner wall of the bin, then downwards along the outer wall of the conical body, and it is sucked into the expanding outer vortex again. Consequently, a secondary circular flow is formed at the top of the dust hopper. Back-mixing flows are also observed at the end of the conical dust outlet, as shown in Fig. 12. A secondary eddy with strong vorticity appears at the outer edge of the expanding vortex. On the other hand, the inner vortex flows upwards in the centre of the dust hopper. When it encounters the down-flowing outer vortex, another secondary eddy with strong vorticity appears at their meeting edge. As a result, a pair of counter-rotating vortices exists at both sides of the expanded down-flowing outer vortex. Separated particles in the outer vortex can be circulated in the dust hopper and be re-entrapped into the inner vortex, then be entrained out of the cyclone. Besides the back-mixing flow, the secondary flow will reduce the separation efficiency of the cyclone.

On the basis of the observation of the flow pattern in this study, the configuration of the dust hopper plays an important role in improving the separation efficiency. A downcomer may be introduced to connect the cyclone conical body and dust bin. The downcomer may facilitate removing the secondary flow, which is a main cause of low collection efficiency of cyclones. Another option may improve the design of the cyclone conical body so as to reduce the back-mixing flow. However, these suggestions were derived from our observations. Further verifications are needed.

5. Conclusions

An experimental method of investigating the three-dimensional swirling flow in a laboratory scale gas cyclone by two-dimensional particle image velocimetry (2D-PIV) technique is presented in this work. Both axial and radial velocities are observed with gas inlet velocity of 7.2–15.0 m/s. The image and displacement distortions caused by the curved cyclone wall have been rectified by a perspective correction scheme. Unfortunately, contamination was introduced into the experimental results due to the existence of considerable out-of-plane (tangential) gas motion in the cyclone. The contamination on the axial velocity has been eliminated efficiently by the proposed methods while that on the radial velocity was difficult to evaluate. The distribution of the radial velocity was then obtained from the local mass balance calculation. In the dust hopper, the back-mixing flow and the secondary flow were observed, as well as a pair of counter-rotating vortices.

Future extension of this work is to investigate the three-dimensional swirling flow in gas cyclones with a stereoscopic (stereo) PIV technique, by which the tangential, axial, and radial velocity fields can be obtained simultaneously. Most importantly, no contamination from the tangential velocity will be introduced into the stereo-PIV results.

Acknowledgements

The authors gratefully acknowledge the financial assistance from AIF, CFI, and NSERC.

References

[1] W. Peukert, C. Wadenpohl, Industrial separation of fine particles with difficult dust properties, Powder Technol. 118 (2001) 136–148.
[2] M.B. Ray, P.E. Luning, A.C. Hoffmann, A. Plomp, M.I.L. Beumer, Improving the removal efficiency of industrial-scale cyclones for particles smaller than five micrometer, Int. J. Miner. Process. 53 (1998) 39–47.
[3] H. Yoshida, K. Fukui, K. Yoshida, E. Shinoda, Particle separation by Iinoya's type gas cyclone, Powder Technol. 118 (2001) 16–23.
[4] K.S. Lim, H.S. Kim, K.W. Lee, Comparative performances of conventional cyclones and double cyclone with and without an electric field, J. Aerosol Sci. 35 (2004) 103–116.
[5] G. Solero, A. Coghe, Experimental fluid dynamic characterization of a cyclone chamber, Exp. Therm. Fluid Sci. 27 (2002) 87–96.
[6] W. Peng, A.C. Hoffmann, P.J.A.J. Boot, A. Udding, H.W.A. Dries, A. Ekker, J. Kater, Flow pattern in reverse-flow centrifugal separators, Powder Technol. 127 (2002) 212–222.
[7] S. Obermair, J. Woisetschläger, G. Staudinger, Investigation of the flow pattern in different dust outlet geometries of a gas cyclone by laser Doppler anemometry, Powder Technol. 138 (2003) 239–251.
[8] L.-Y. Hu, L.-X. Zhou, J. Zhang, M.-X. Shi, Studies on strongly swirling flows in the full space of a volute cyclone separator, AIChE J. 51 (2005) 740–749.
[9] H.F. Meier, M. Mori, Anisotropic behavior of the Reynolds stress in gas and gas–solid flows in cyclones, Powder Technol. 101 (1999) 108–119.
[10] A.C. Hoffmann, M. de Groot, A. Hospers, The effect of the dust collection system on the flowpattern and separation efficiency of a gas cyclone, Can. J. Chem. Eng. 74 (1996) 464–470.
[11] W.D. Griffiths, F. Boysan, Computational fluid dynamics (CFD) and empirical modeling of the performance of a number of cyclone samplers, J. Aerosol Sci. 27 (1996) 281–304.
[12] A.J. Hoekstra, J.J. Derksen, H.E.A. Van Den Akker, An experimental and numerical study of turbulent swirling flow in gas cyclones, Chem. Eng. Sci. 54 (1999) 2055–2065.
[13] A.K. Gupta, D.G. Lilley, N. Syred, Swirling Flows, Abacus Press, Tunbridge Wills, UK, 1984.
[14] D.J. Brandon, S.K. Aggarwal, A numerical investigation of particle deposition on a square cylinder placed in a channel flow, Aerosol Sci. Technol. 34 (2001) 340–352.
[15] L.-Y. Hu, M.-X. Shi, Three-dimensional time-averaged flow structure in cyclone separator with volute inlet, J. Chem. Ind. Eng. 54 (2003) 549–556 (in Chinese).
[16] Z.-L. Liu, Y. Zheng, L.-F. Jia, J.-Y. Jiao, Q.-K. Zhang, Stereoscopic PIV studies on the swirling flow structure in a gas cyclone, Chem. Eng. Sci. 61 (2006) 4252–4261.